Experimental set-up for determination of the large-strain tensile behaviour of polymers at low temperatures

Joakim Johnsen[a,*], Frode Grytten[b], Odd Sture Hopperstad[a], Arild Holm Clausen[a]

[a]*Structural Impact Laboratory (SIMLab), Department of Structural Engineering, NTNU, Norwegian University of Science and Technology, NO-7491 Trondheim, Norway*
[b]*SINTEF Materials and Chemistry, Department of Materials and Nanotechnology, PB 124 Blindern, NO-0314 Oslo, Norway*

Abstract

In this study, we present a method to determine the large-strain tensile behaviour of polymers at low temperatures using a purpose-built temperature chamber made of polycarbonate (PC). This chamber allows for several cameras during testing. In our case, two digital cameras were utilized to monitor the two perpendicular surfaces of the test sample. Subsequently, the pictures were analysed with digital image correlation (DIC) software to determine the strain field on the surface of the specimen. In addition, a thermal camera was used to monitor self-heating during loading. It is demonstrated that the PC chamber does not influence the stress-strain curve as determined by DIC. Applying this set-up, a semi-crystalline cross-linked low-density polyethylene (XLPE) under quasi-static tensile loading has been successfully analysed using DIC at four different temperatures (25 °C, 0 °C, −15 °C, −30 °C). At the lower temperatures, the conventional method of applying a spray-paint speckle failed due to embrittlement and cracking of the spray-paint speckle when the tensile specimen deformed. An alternative method was developed utilising white grease with a black powder added as contrast. The results show a strong increase in both the Young's modulus and the flow stress for decreasing temperatures within the experimental range. We also observe that although the XLPE material is practically incompressible at room temperature, the volumetric strains reach a value of about 0.1 at the lower temperatures.

Keywords: XLPE, Digital image correlation (DIC), Tensile test, Low temperatures, Large strains, Polymeric material, Temperature chamber

1. Introduction

Polymeric materials are used in a variety of applications in the oil industry, e.g. thermal insulation coatings of pipelines, pressure barriers, and insulation of umbilical cables. Estimates from The United States Geological Survey (USGS) indicate that large amounts of the world's undiscovered oil and gas resources are located north of the Arctic Circle [1]. Consequently, the material behaviour at low temperatures is of increasing interest for the oil industry. The effect of temperature on the material behaviour needs to be understood for different complex load cases, such as reeling/unreeling of pipelines, and impact on various structures and components involving polymeric materials. It is therefore necessary to obtain reliable material data even at lower temperatures, because a reduction in temperature tends to

reduce the ductility. Relevant input, such as true stress-strain curves for large deformations, volumetric strain to incorporate damage, temperature to include material softening, and rate effects on flow stress, is needed for the material models implemented in finite element (FE) software to predict the material response as accurately as possible. It is therefore essential to obtain precise data at large deformations from experiments in order to analyse such complex load cases successfully.

Several studies have been conducted addressing the performance of polymeric materials at elevated temperatures [2–8]. Fewer studies have been carried out with emphasis on the material behaviour at low temperatures, in particular with attention to the material response at large strains. Bauwens and Bauwens-Crowet with co-workers [9–12] published a series of papers on the relation between yield stress and temperature. Jang et al. [13] investigated the ductile-brittle transition in polypropylene and reported relevant stress-strain data.

---

*Corresponding author
Email address: joakim.johnsen@ntnu.no (Joakim Johnsen)

Şerban et al. [14], Brown et al. [15] and Cao et al. [16] conducted uniaxial tensile experiments on different polymers using an incremental extensometer. In addition, Richeton et al. [17] determined true stress-strain compression data for three different materials at −40 °C using a deflectometer. Common for all the mentioned studies investigating the material response at low temperatures is that they have used a non-transparent temperature chamber, relying on mechanical measuring devices to calculate the strains instead of optical alternatives, like for example digital image correlation (DIC).

A typical feature with uniaxial tension and compression tests on polymers is that the stress and strain fields remain homogeneous only for small deformations. Localization occurs at the onset of necking in a tension test, meaning that the stress and strain fields become heterogeneous. After this stage, extensometer data are no longer useful and DIC, or another method for local measurement of the deformation in the neck, is needed to obtain the true stress-strain relationship. Another argument for instrumenting material tests on polymers with cameras for subsequent DIC analysis, is that such materials are susceptible to volume change during plastic deformation. Hence, the transverse strains have to be measured in order to calculate the true stress. It follows that DIC is an essential tool to extract accurate data from mechanical tests of polymers [14, 18–22].

Given that the material is isotropic, one can make due with only one DIC camera, while transversely anisotropic materials call for determination of both transverse strain components, and two cameras are required. Strong curvature of the deformed section would also normally call for two cameras and stereo (3D) DIC [23–25]. This issue is considered in Section 3.1.

In the present work, a temperature chamber was made of transparent polycarbonate (PC) to allow two digital cameras and a thermal camera to monitor the tensile specimens during experiments. The two digital cameras were mounted in two perpendicular directions, while a rectangular slit was added in one of the temperature chamber walls to obtain a free line-of-sight between the thermal camera and the test sample. The images obtained from the two digital cameras were analysed using DIC to obtain the strain fields on the two surfaces of the sample. As shown in the tests at low temperatures reported by Ilseng et al. [26], the usual spray-paint speckle, which is required for DIC analysis after the test, became brittle and cracked under deformation at low temperatures, rendering DIC analysis impossible. To remedy this a low temperature white grease (Molykote 33 Medium [27]) was applied evenly onto the specimen surface, and the speckle was added in the

form of a black powder with a grain size between 75 μm and 125 μm.

2. Material and method

2.1. Material

The material, an extruded cross-linked low-density polyethylene (XLPE), was supplied by Nexans Norway as 128 mm long cable segments with an external diameter of 73 mm and a thickness of 21 mm. It was produced by Borealis under the product name Borlink LS4201S [28], a semi-crystalline thermoset polymer intended for use as electrical insulation of high-voltage cables, e.g. electric cables connecting the offshore platform to an onshore power plant.

2.2. Tensile specimen

The tensile specimen, see Figure 1, was designed by Andersen [29]. For evaluation of the true stress-strain
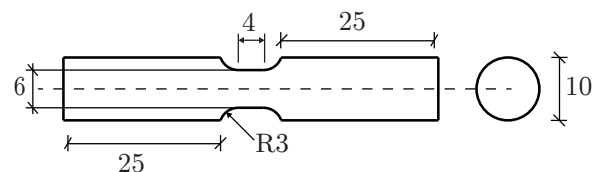

Figure 1: Tensile specimen used in the experiments. All measures in mm.

response at large deformations the circular cross-section is favourable to the rectangular specimen proposed in ISO 527-2:2012 [30] since (i) it removes the stress concentrations imposed by the comparatively stiff corners, (ii) the overall shape of the most strained cross-section is better maintained throughout the test, and (iii) it facilitates estimation of a Bridgman-corrected equivalent stress provided that the deformed contour can be tracked from the digital images. Another important aspect of the specimen design is the relatively short gauge length. This increases the resolution of the images used in the DIC analysis by allowing the digital cameras to capture a smaller area, thus facilitating accurate measurements of logarithmic strains approaching a magnitude of 2.0.

The specimens were machined in a turning lathe from sections cut in the longitudinal direction of an extruded cable insulation with dimensions 128 mm × 73 mm × 21 mm (length × diameter × thickness). To ensure that the DIC cameras monitored the same material orientations in each experiment, the thickness direction of the extruded cable insulation was marked on the tensile specimens. The perpendicular direction thus corresponds to the hoop direction of the cable insulation.

2.3. Temperature chamber

Regular temperature chambers are often fitted with only one window, see e.g. [31, 32]. This complicates the use of two digital cameras to monitor the specimen during experiments for later DIC analysis since the cameras must be mounted close together, see e.g. Grytten et al. [18]. Additionally, it is not feasible to obtain a free line-of-sight between the test sample and a thermal camera, making it impossible to measure any self-heating using infrared devices. Our temperature chamber however, shown in Figure 2, allows for this. The chamber was
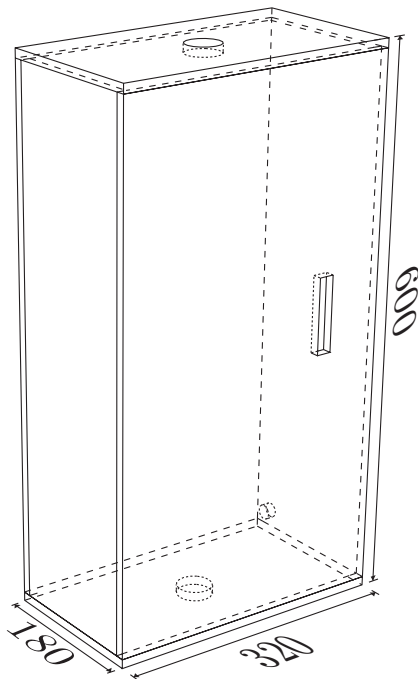
Figure 2: Temperature chamber used in the experiments. All measures in mm.

built of 10 mm thick plates made of transparent polycarbonate, produced by SABIC Innovative Plastics under the product name Lexan Exell D [33]. The material and solution are similar to the one used by Børvik et al. [34]. The transparency of the chamber in Figure 2 allowed several digital cameras to monitor the specimen. A rectangular slit was added in the front window of the temperature chamber to obtain a free line-of-sight between a thermal camera and the tensile specimen. The temperature in the chamber was governed by a thermocouple temperature sensor controlling the flow of liquid nitrogen through the small hole in one of the narrow side walls of the chamber. To ensure that the desired temperature was obtained at the most critical cross-section of the tensile specimen, the sensor was mounted close to

the gauge section.

Circular holes were added in the top and in the bottom of the chamber to allow mounting of the test specimen in the tensile rig without impairing the seal of the chamber.

2.4. Experimental set-up

The test set-up is illustrated in Figures 3 and 4. In addition to the temperature chamber and an Instron 5944 testing machine with a 2 kN load cell, it involves two Prosilica GC2450 cameras equipped with Sigma 105 mm and Nikon 105 mm macrolenses. Both cameras were positioned at a distance of approximately 25-35 cm from the tensile specimen, giving a resolution of roughly 60 pixels/mm. The two cameras were used to
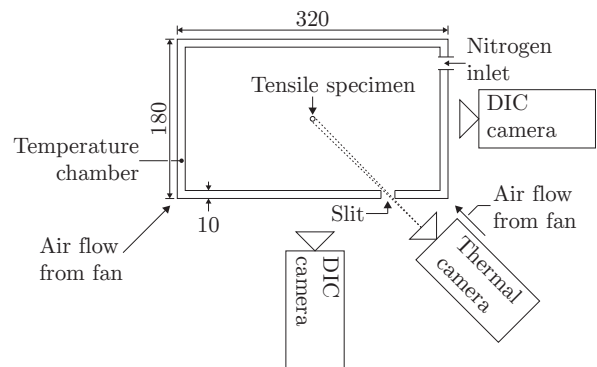

Figure 3: Section view of the set-up used in the experiments. All measures in mm. The distance to the three cameras is not drawn in scale.

measure the transverse strain in both the thickness direction and the hoop direction of the cable insulation, in addition to the longitudinal strain. Moreover, a FLIR
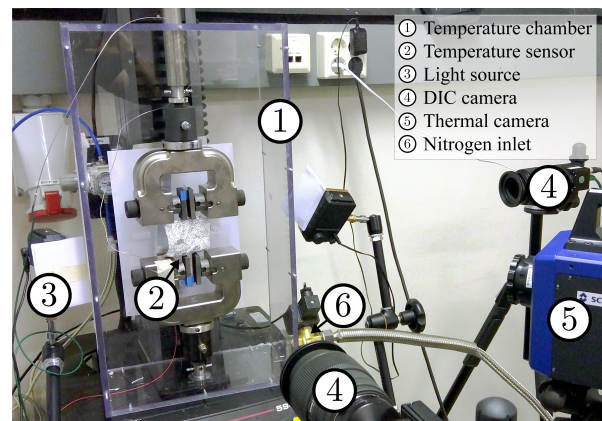

Figure 4: Picture showing the experimental set-up. Note that neither the front window nor the tensile specimen is mounted.

SC 7500 thermal camera was used to measure any possible self-heating in the specimen during the test. It also served to check that the surface temperature of the sample was the same as the gas temperature in the chamber.

Traditionally, a spray paint is used to apply a random black and white speckle which deforms along with the specimen. This deformation is monitored by the DIC cameras and transformed into strain by correlating the current deformed speckle to a reference. However, when the temperature drops, the spray paint becomes brittle and cracks even at relatively small strains, as illustrated in Figure 5. To prevent this, the spray paint was replaced by white grease, with black powder added to follow the deformation, see Figure 5. The black powder had a grain size from 75 μm to 125 μm. This set-up showed no signs of cracking, even at large strains.
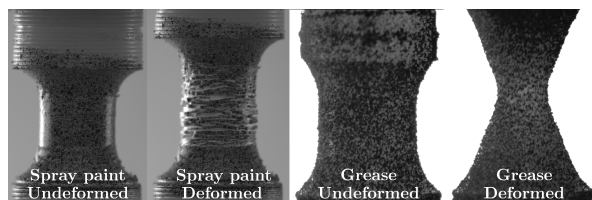

Figure 5: Image series illustrating the superior performance of grease compared to the conventional spray-paint speckle at −30 °C.

In the preliminary experiments there were also problems with icing due to condensation on the outside of the chamber. The solution was to mount fans in the positions indicated in Figure 3. The continuous flow of air over the transparent walls of the chamber successfully prevented condensation and icing.

The tensile tests were carried out at four different temperatures; 25 °C, 0 °C, −15 °C and −30 °C; with two repetitions per test configuration. All experiments were conducted at an initial nominal strain rate of 10^{-2} s^{-1}, translating to a cross-head velocity of 2.4 mm/min.

2.5. Thermal conditioning

A thermal analysis was performed in Abaqus [35] to estimate the required cooling time for the specimens before they reached the lowest temperature of −30 °C. The laser flash method [36] was used to determine the thermal conductivity k and the specific heat capacity C_p needed as input to the analysis. Five cylindrical samples with a diameter of 12.7 mm and a thickness of 0.5 mm were tested at three temperatures: 25 °C, 35 °C and 50 °C. Due to limitations in the testing apparatus, it was not possible to perform tests below room temperature. As seen in Figure 6, the thermal conductivity is more or

less constant, although with some scatter, while the specific heat capacity varies linearly with temperature. The mean value of the test results at room temperature was used as input to the thermal analysis. It is noted that it is conservative with respect to cooling time to apply a high value of C_p in the numerical simulation.
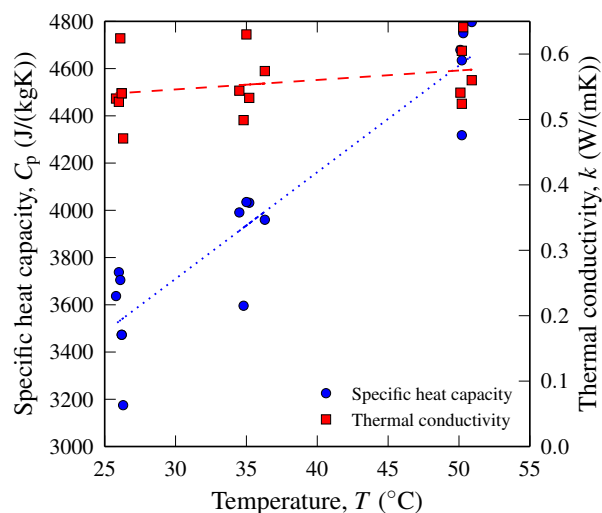

Figure 6: Specific heat capacity C_p and thermal conductivity k plotted against temperature.

The coefficient of heat convection to air h_c was estimated by first heating a small cylindrical sample with dimensions 20 mm × 5 mm (diameter × height) in boiling water, followed by monitoring the temperature decrease in the specimen using an infrared thermometer. From the recorded temperature history the heat convection to air was found to be about 21 W/(m²K).

A 3D model of the tensile specimen was made in Abaqus, consisting of 51728 DC3D8 elements. Input parameters used in the Abaqus analysis are given in Table 1. The interior of the specimen was given an initial temperature of 25 °C, while at the exterior a thermal boundary condition of −30 °C was applied as a surface film. Analysis results showed that a preconditioning time of 30 min was sufficient to cool the specimen. Thus, each sample was put in the chamber 30 min before it was tested.

2.6. Determination of true stress and logarithmic strain

True stress, σ, is defined as

$$\sigma = \frac{F}{A} \qquad (1)$$

where F is the applied force and A is the current cross-section area. The current cross-section area is calculated

4

Table 1: Input parameters used in thermal analysis.

Specific heat capacity, C_p (J/(kgK))	Thermal conductivity, k (W/(mK))	Heat convection to air, h_c (W/(m^{2}K))	Density, ρ (kg/m^3)
3546	0.56	21.0	922

from the assumption that the transverse stretches in the thickness direction and in the hoop direction of the cable insulation represent the stretches along the minor and major axis of an elliptical cross-section, i.e.:

$$A = \pi \lambda_T \lambda_\perp r_0^2 \qquad (2)$$

where $\lambda_T = r_T/r_0$ is the stretch in the thickness direction, $\lambda_\perp = r_\perp/r_0$ is the stretch in the hoop direction and r_0 is the initial radius of the undeformed specimen in the gauge area. The transverse stretches in both the thickness direction and the hoop direction are calculated as the average value over the cross-section in the neck.

The images from the tensile tests were post-processed using an in-house DIC software [29] written in MATLAB [37]. From this software we obtain the deformation gradient $\mathbf{F}$, which enables the calculation of the stretch tensor $\mathbf{U}$ from the polar decomposition $\mathbf{F} = \mathbf{RU}$. Now we can calculate the logarithmic strain tensor by taking the logarithm of the stretch tensor, viz.

$$\boldsymbol{\epsilon} = \ln(\mathbf{U}) = \mathbf{N} \ln(\hat{\mathbf{U}}) \mathbf{N}^T \qquad (3)$$

where $\mathbf{N}$ contains the eigenvectors of $\mathbf{U}$ and $\hat{\mathbf{U}}$ is the eigentensor. Note that for uniaxial tension $\mathbf{U} = \hat{\mathbf{U}}$ such that

$$\boldsymbol{\epsilon} = \begin{bmatrix} \epsilon_L & 0 & 0 \\ 0 & \epsilon_T & 0 \\ 0 & 0 & \epsilon_\perp \end{bmatrix} = \begin{bmatrix} \ln(\lambda_L) & 0 & 0 \\ 0 & \ln(\lambda_T) & 0 \\ 0 & 0 & \ln(\lambda_\perp) \end{bmatrix} \qquad (4)$$

where $\lambda_L = L/L_0$ is the longitudinal stretch.

The logarithmic volumetric strain is defined as the trace of the logarithmic strain tensor. However, as the logarithmic strain tensor estimated here represents an average over the gauge volume, it has been found necessary to correct the volumetric strain for the non-uniformity of the strain field. An appropriate correction was proposed by Andersen [29], which takes the heterogeneity of the longitudinal strain in the neck into account. The corrected volumetric strain reads

$$\epsilon_{V,corr} = \ln\left(\frac{V}{V_0}\right) = \ln\left[\lambda_L \lambda_T \lambda_\perp \cdot \left(1 + \frac{\kappa R}{4}\right)\right] \qquad (5)$$

$$= \text{tr}(\boldsymbol{\epsilon}) + \ln\left(1 + \frac{\kappa R}{4}\right)$$

where κ is the external curvature of the neck, and R is the current radius in the neck. The current values of κ and R are found from the digital images taken during the tests. This correction removes the unphysical negative volumetric strain in the beginning of the tension test, as shown in Section 3.3.

3. Results and discussion

3.1. Evaluation of experimental set-up

When the tensile specimen deforms, and eventually necks, the surface of the sample translates and rotates in the out-of-plane direction. A quasi-static tensile test was conducted at room temperature to compare the calculated strains from 2D DIC and 3D DIC. An in-house DIC software [29] applying a higher-order element for description of the deformation field, was employed in the 2D case. The analysis with 3D DIC was carried out using the in-house DIC software eCorr [38].
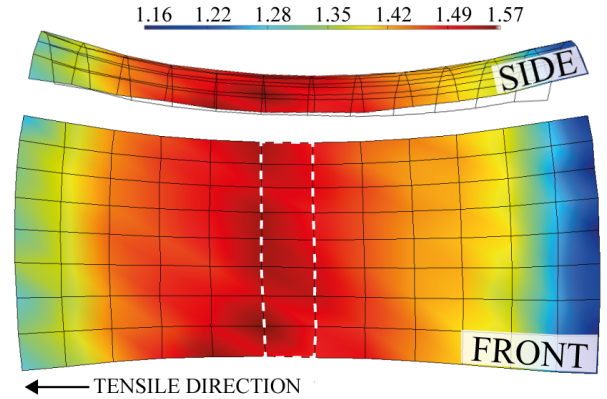

Figure 7: Front and side view of the 3D DIC mesh at a maximal stretch in the neck of about 1.55. The elements used in the strain calculations are highlighted by the white box.

Based on the DIC analysis we obtain the displacement field $\mathbf{u}$, enabling the calculation of the deformation gradient $\mathbf{F}$. From the deformation gradient the strains are calculated following the procedure outlined in Section 2.6. The interested reader is referred to Fagerholt et al. [39, 40] for a thorough explanation of how the displacement field $\mathbf{u}$ is found from the digital images.

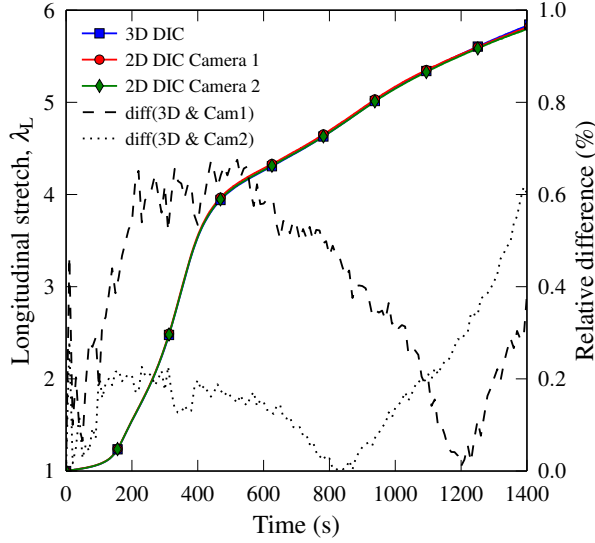The representative strain was calculated from the average value of the longitudinal stretch for the elements

Figure 8: Comparison of longitudinal stretch for XLPE calculated by 3D and 2D DIC. The dashed lines give the relative percentage difference between 3D DIC and 2D DIC for camera 1 and camera 2.

Figure 9: True stress vs. logarithmic strain for the three benchmark tests performed on a polypropylene copolymer material.

highlighted in Figure 7. Figure 8 shows that the difference between 2D (both cameras) and 3D DIC remains below 1.0% during the experiment, meaning that the error introduced in 2D DIC by the out-of-plane translation of the specimen during deformation is acceptable. Therefore 2D DIC was chosen for the subsequent data processing.

To verify that there was no influence on the DIC results neither by the replacement of spray-paint with grease nor by introducing the polycarbonate window between the cameras and the sample, three tests were conducted at room temperature on a rubber modified polypropylene (PP) material: First a test with a traditional spray-paint speckle, then a test with the spray-paint speckle behind a polycarbonate window, and finally a test where the spray-paint speckle was replaced with white grease and black powder. Using the transverse strains and the relation $\lambda_i = \exp(\epsilon_i)$, the true stress was calculated following the procedure given in Section 2.6. The DIC analyses of the three tests revealed only negligible differences, illustrated by the three stress-strain curves in Figure 9 and the three curves representing the trace of the logarithmic strain tensor versus the logarithmic longitudinal strain in Figure 10.

3.2. Stress-strain behaviour at different temperatures

The transverse strains, ϵ_t, as a function of longitudinal strain at room temperature are shown in Figure 11 for the XLPE material, where ϵ_t is either equal to
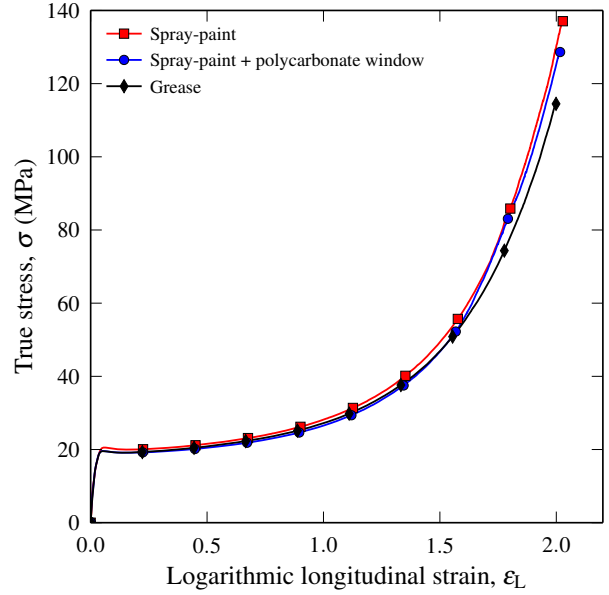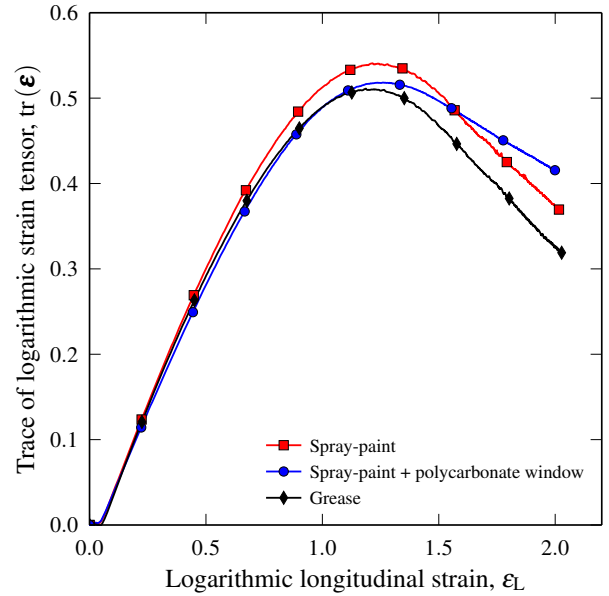

Figure 10: Trace of the logarithmic strain tensor vs. logarithmic longitudinal strain for the three benchmark tests performed on a polypropylene copolymer material.

ϵ_T or $\epsilon_\perp$. Both transverse strains have a close to linear relation with the longitudinal strain, but with different slopes. This quasi-linear relation is also reflected in the moderate variation of the transverse strain ratios $r = \epsilon_\perp / \epsilon_T$ shown in the same figure, which lies between approximately 1.1 and 1.0 for the four inves-

6

tigated temperatures. These results demonstrate the transverse anisotropy of XLPE and the necessity of using two cameras to capture this effect.
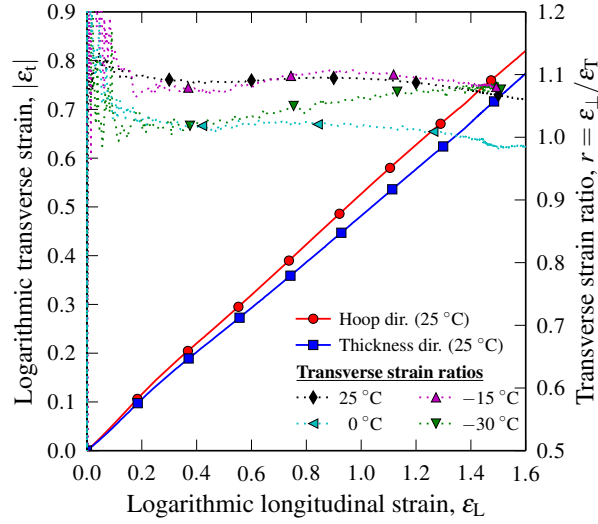

Figure 11: Logarithmic transverse strain for XLPE in the hoop ($\perp$) and in the thickness direction (T) at room temperature, and the transverse strain ratios for all investigated temperatures plotted against logarithmic longitudinal strain.

The stress-strain curves for XLPE at the four investigated temperatures are presented in Figure 12, where the true stress is calculated with Equations 1 and 2. It appears that the Young's modulus and the flow stress increase with decreasing temperature. Another observation from Figure 12 is that the ductility of the material is more or less independent of temperature in the experimental range, making it well suited for low temperature applications. The uniaxial tension tests performed at $-15\,°C$ and $-30\,°C$ have a fracture strain of about 1.4, while the fracture strain in the tests carried out at $0\,°C$ and $25\,°C$ is roughly 1.6, i.e., 14% increase compared to the two lower temperatures. It is however noted that the network hardening occurring at strains larger than approximately 1.3 is less prominent at the two lowest temperatures, and that the initial strain hardening clearly has increased compared to the two highest temperatures.

Both the flow stress, σ_{20}, defined as the stress magnitude at a longitudinal strain of 0.2 (= 20%), and the initial stiffness, E, can be represented through the exponential relations

$$E(\theta) = E_0 \exp(a/\theta) \qquad (6)$$
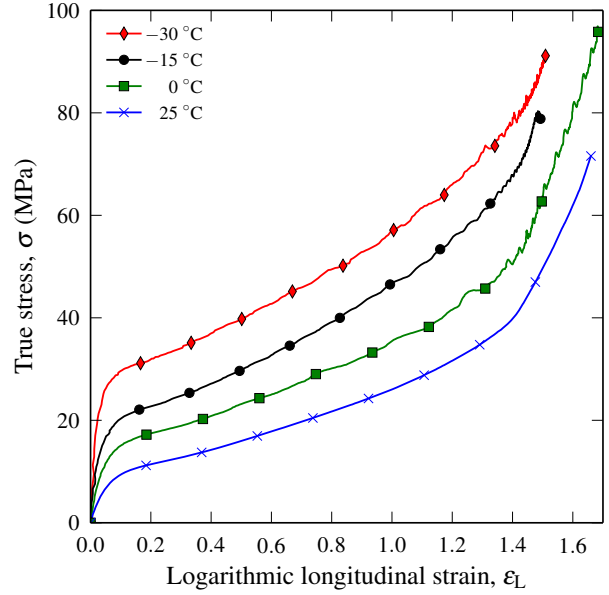$$\sigma_{20}(\theta) = C \exp(b/\theta) \qquad (7)$$

Figure 12: True stress vs. logarithmic longitudinal strain for XLPE at different temperatures.

where a, b, E_0 and C are material parameters and θ is the absolute temperature. Figure 13 shows the calculated Young's modulus and flow stress versus temperature as well as the least square fits of Equations 6 and 7. Note that these expressions are valid only for the investigated temperature range.
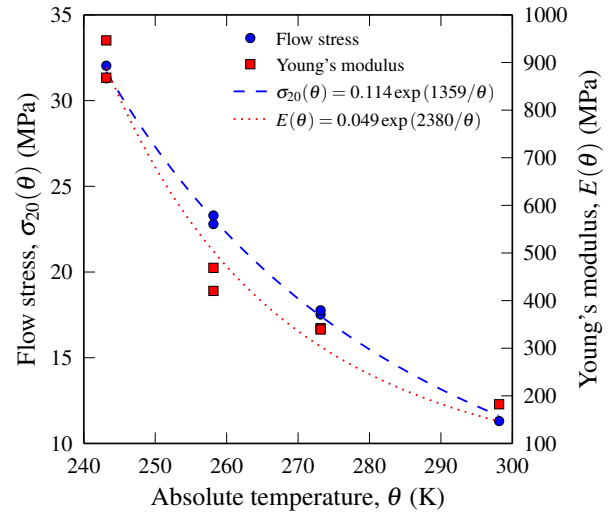

Figure 13: Evolution of flow stress and Young's modulus as a function of temperature for XLPE.

3.3. Volumetric strains at different temperatures

The logarithmic volumetric strain for XLPE calculated as the trace of the logarithmic strain tensor is given in Figure 14, while the corrected volumetric strain calculated according to Equation 5 is given in Figure 15. Since the grease was applied by hand, it was impos-
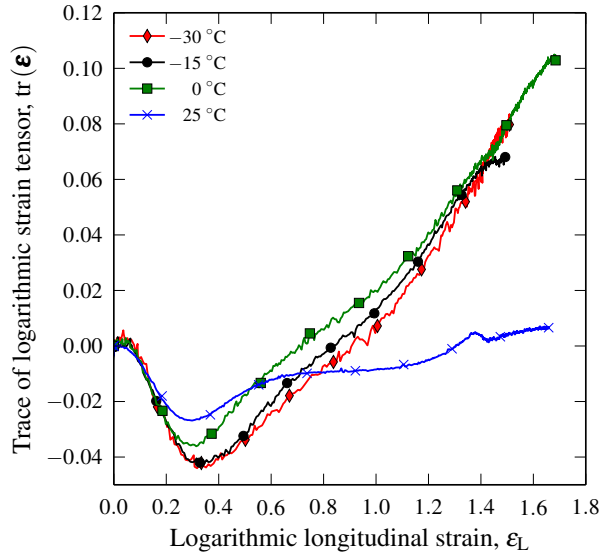

Figure 14: Trace of the logarithmic strain tensor vs. logarithmic longitudinal strain for XLPE.

sible to distribute it completely evenly over the gauge section. This made it difficult to approximate the curvature, κ, by tracing the edges of the specimen, which is needed in Equation 5. As an alternative method, we chose to fit a second-order polynomial to the element boundaries of the DIC mesh, and to calculate the curvature by taking the second-order derivative of this polynomial. Since the curvature is zero in the cold drawing phase at the end of the test (Figure 16), this approximation will not affect the final volumetric strain, but it removes the unphysical negative volumetric strain seen in Figure 14. This approximation of the curvature might be the explanation for the minor difference between the volumetric strain at small ϵ_L for the test performed at $-15\ °C$ and the tests at $0\ °C$ and $-30\ °C$ in Figure 15. Nevertheless, in both figures we see that the volumetric strain increases for the lower temperatures compared to the response at room temperature where the volumetric strain is close to 0 at all deformation levels. Since there was no stress whitening during deformation, and this material is tailored to include as few free particles as possible, it is not obvious that the increase in volumetric strain is caused by material damage. However, how much of this volumetric strain that is recoverable has not
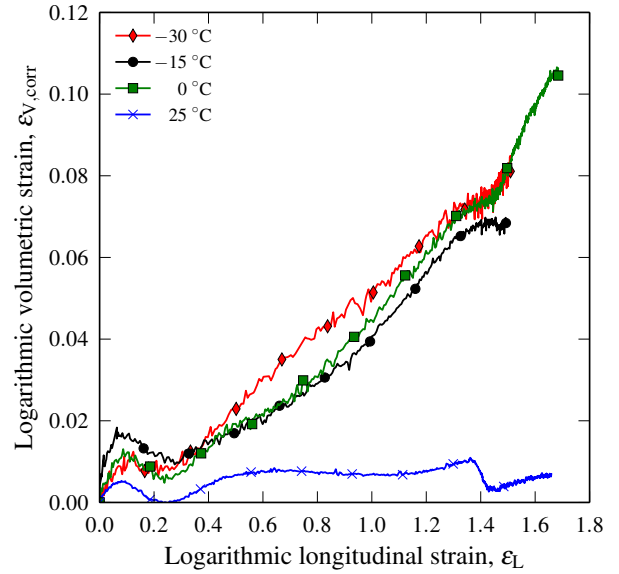

Figure 15: Corrected logarithmic volumetric strain using Equation 5 vs. logarithmic longitudinal strain for XLPE.
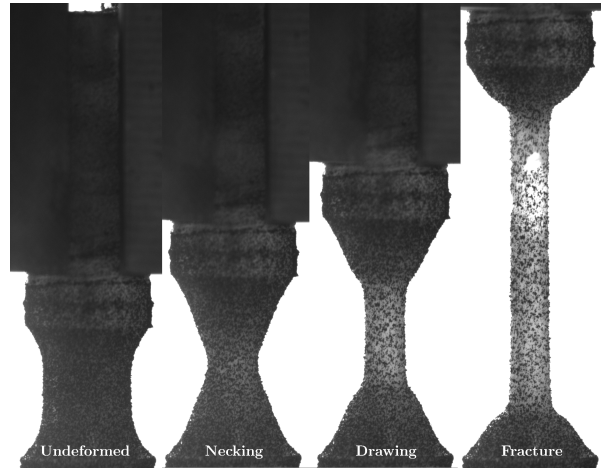

Figure 16: Time lapse showing the deformation history of the tensile specimen.

been investigated. Therefore, it would be interesting to perform loading/unloading tests at lower temperatures in further work.

3.4. Self-heating at different temperatures

The temperature data recorded by the thermal camera showed no significant self-heating of the specimen at the applied nominal strain rate of $10^{-2}\ s^{-1}$, indicating isothermal loading conditions. However, if the experiments had been conducted at higher strain rates, there would most likely have been a substantial temperature increase in the specimen. This experimental

set-up could provide important input to any numerical model incorporating thermal softening.

4. Concluding remarks

A non-contact optical method for determining the large-strain tensile behaviour of polymers at low temperatures has been presented. The method successfully enables multiple DIC camera instrumentation during experiments, as well as the possibility to monitor self-heating in the specimen using a thermal camera. Since any temperature increase in the material due to self-heating introduces material softening, the ability to measure this using for instance a thermal camera is highly relevant for the development of material models to be used in numerical simulations.

The experimental set-up enables calculation of the true stress vs. logarithmic strain curve and the volumetric strain at low temperatures. Although the XLPE material exhibits rather small volumetric strain, this is not necessarily the case for all polymeric materials. In addition to this, the ability to monitor self-heating underlines the relevance of the presented experimental set-up, especially when considering how important volumetric strain and self-heating is in material models that include damage and thermal softening.

The investigated material (XLPE) exhibits an exponential increase in both the initial stiffness and the flow stress when the temperature is reduced within the experimental range. In addition, the reduction of temperature changes the material from nearly incompressible at room temperature to compressible at lower temperatures.

5. Acknowledgements

References

[1] D. L. Gautier, K. J. Bird, R. R. Charpentier, A. Grantz, D. W. Houseknecht, T. R. Klett, T. E. Moore, J. K. Pitman, C. J. Schenk, J. H. Schuenemeyer, K. Sørensen, M. E. Tennyson, Z. C. Valin, C. J. Wandrey, Assessment of undiscovered oil and gas in the arctic, Science 324 (5931) (2009) 1175–1179.

[2] E. M. Arruda, M. C. Boyce, R. Jayachandran, Effects of strain rate, temperature and thermomechanical coupling on the finite strain deformation of glassy polymers, Mechanics of Materials 19 (2-3) (1995) 193–212. `doi:10.1016/0167-6636(94)00034-E`.

[3] J. Zaroulis, M. Boyce, Temperature, strain rate, and strain state dependence of the evolution in mechanical behaviour and structure of poly(ethylene terephthalate) with finite strain deformation, Polymer 38 (6) (1997) 1303–1315. `doi:10.1016/S0032-3861(96)00632-5`.

[4] L. C. A. Van Breemen, T. A. P. Engels, E. T. J. Klompen, D. J. A. Senden, L. E. Govaert, Rate- and temperature-dependent strain softening in solid polymers, Journal of Polymer Science, Part B: Polymer Physics 50 (24) (2012) 1757–1771. `doi:10.1002/polb.23199`.

[5] F. Zaïri, M. Naït-Abdelaziz, J. M. Gloaguen, J. M. Lefebvre, Constitutive modelling of the large inelastic deformation behaviour of rubber-toughened poly(methyl methacrylate): effects of strain rate, temperature and rubber-phase volume fraction, Modelling and Simulation in Materials Science and Engineering 18 (5) (2010) 055004. `doi:10.1088/0965-0393/18/5/055004`.

[6] M. Nasraoui, P. Forquin, L. Siad, A. Rusinek, Influence of strain rate, temperature and adiabatic heating on the mechanical behaviour of poly-methyl-methacrylate: Experimental and modelling analyses, Materials and Design 37 (2012) 500–509. `doi:10.1016/j.matdes.2011.11.032`.
URL `http://dx.doi.org/10.1016/j.matdes.2011.11.032`

[7] V. Srivastava, S. A. Chester, N. M. Ames, L. Anand, A thermo-mechanically-coupled large-deformation theory for amorphous polymers in a temperature range which spans their glass transition, International Journal of Plasticity 26 (8) (2010) 1138–1182. `doi:10.1016/j.ijplas.2010.01.004`.
URL `http://dx.doi.org/10.1016/j.ijplas.2010.01.004`

[8] P. Llana, M. Boyce, Finite strain behavior of poly(ethylene terephthalate) above the glass transition temperature, Polymer 40 (24) (1999) 6729–6751. `doi:10.1016/S0032-3861(98)00867-2`.

[9] C. Bauwens-Crowet, J. C. Bauwens, G. Homs, Tensile yield-stress behavior of glassy polymers, Journal of Polymer Science Part A-2: Polymer Physics 7 (4) (1969) 735–742. `doi:10.1002/pol.1969.160070411`.

[10] C. Bauwens-Crowet, J. C. Bauwens, G. Homès, The temperature dependence of yield of polycarbonate in uniaxial compression and tensile tests, Journal of Materials Science 7 (2) (1972) 176–183. `doi:10.1007/BF00554178`.

[11] J. C. Bauwens, Relation between the compression yield stress and the mechanical loss peak of bisphenol-A-polycarbonate in the β transition range, Journal of Materials Science 7 (5) (1972) 577–584. `doi:10.1007/BF00761956`.

[12] C. Bauwens-Crowet, The compression yield behaviour of poly-methyl methacrylate over a wide range of temperatures and strain-rates, Journal of Materials Science 8 (7) (1973) 968–979. `doi:10.1007/BF00756628`.

[13] B. Z. Jang, D. R. Uhlmann, J. B. V. Sande, Ductilebrittle tran-

sition in polymers, Journal of Applied Polymer Science 29 (11) (1984) 3409–3420. `doi:10.1002/app.1984.070291118`.

[14] D. A. Şerban, G. Weber, L. Marşavina, V. V. Silberschmidt, W. Hufenbach, Tensile properties of semi-crystalline thermoplastic polymers: Effects of temperature and strain rates, Polymer Testing 32 (2) (2013) 413–425. `doi:10.1016/j.polymertesting.2012.12.002`.

[15] E. N. Brown, P. J. Rae, E. B. Orler, The influence of temperature and strain rate on the constitutive and damage responses of polychlorotrifluoroethylene (PCTFE, Kel-F 81), Polymer 47 (21) (2006) 7506–7518. `doi:10.1016/j.polymer.2006.08.032`.

[16] K. Cao, Y. Wang, Y. Wang, Effects of strain rate and temperature on the tension behavior of polycarbonate, Materials and Design 38 (2012) 53–58. `doi:10.1016/j.matdes.2012.02.007`.
URL `http://dx.doi.org/10.1016/j.matdes.2012.02.007`

[17] J. Richeton, S. Ahzi, K. Vecchio, F. Jiang, R. Adharapurapu, Influence of temperature and strain rate on the mechanical behavior of three amorphous polymers: Characterization and modeling of the compressive yield stress, International Journal of Solids and Structures 43 (7-8) (2006) 2318–2335. `doi:10.1016/j.ijsolstr.2005.06.040`.

[18] F. Grytten, H. Daiyan, M. Polanco-Loria, S. Dumoulin, Use of digital image correlation to measure large-strain tensile properties of ductile thermoplastics, Polymer Testing 28 (6) (2009) 653–660. `doi:10.1016/j.polymertesting.2009.05.009`.
URL `http://linkinghub.elsevier.com/retrieve/pii/S0142941809000853`

[19] V. Delhaye, A. H. Clausen, F. Moussy, R. Othman, O. S. Hopperstad, Influence of stress state and strain rate on the behaviour of a rubber-particle reinforced polypropylene, International Journal of Impact Engineering 38 (4) (2011) 208–218. `doi:10.1016/j.ijimpeng.2010.11.004`.
URL `http://dx.doi.org/10.1016/j.ijimpeng.2010.11.004`

[20] A. S. Ognedal, A. H. Clausen, M. Polanco-Loria, A. Benallal, B. Raka, O. S. Hopperstad, Experimental and numerical study on the behaviour of PVC and HDPE in biaxial tension, Mechanics of Materials 54 (2012) 18–31. `doi:10.1016/j.mechmat.2012.05.010`.
URL `http://linkinghub.elsevier.com/retrieve/pii/S0167663612001123`

[21] M. Jerabek, Z. Major, R. W. Lang, Strain determination of polymeric materials using digital image correlation, Polymer Testing 29 (3) (2010) 407–416. `doi:10.1016/j.polymertesting.2010.01.005`.
URL `http://dx.doi.org/10.1016/j.polymertesting.2010.01.005`

[22] S. R. Heinz, J. S. Wiggins, Uniaxial compression analysis of glassy polymer networks using digital image correlation, Polymer Testing 29 (8) (2010) 925–932. `doi:10.1016/j.polymertesting.2010.08.001`.
URL `http://dx.doi.org/10.1016/j.polymertesting.2010.08.001`

[23] G. Besnard, F. Hild, J.-M. Lagrange, P. Martinuzzi, S. Roux, Analysis of necking in high speed experiments by stereocorrelation, International Journal of Impact Engineering 49 (2012) 179–191. `doi:10.1016/j.ijimpeng.2012.03.005`.
URL `http://dx.doi.org/10.1016/j.ijimpeng.2012.03.005`

[24] A. Gilat, T. E. Schmidt, A. L. Walker, Full Field Strain Measurement in Compression and Tensile Split Hopkinson Bar Experiments, Experimental Mechanics 49 (2009) 291–302. `doi:`

[25] M. A. Sutton, J. H. Yan, V. Tiwari, H. W. Schreier, J. J. Orteu, The effect of out-of-plane motion on 2D and 3D digital image correlation measurements, Optics and Lasers in Engineering 46 (10) (2008) 746–757. `doi:10.1016/j.optlaseng.2008.05.005`.

[26] A. Ilseng, B. H. Skallerud, A. H. Clausen, Tension behaviour of HNBR and FKM elastomers for a wide range of temperatures, Polymer Testing 49 (2016) 128–136. `doi:10.1016/j.polymertesting.2015.11.017`.
URL `http://dx.doi.org/10.1016/j.polymertesting.2015.11.017`

[27] Molykote 33 Extreme Low Temp. Bearing Grease, Medium, `https://www.dowcorning.com/applications/search/products/Details.aspx?prod=01889788&type=PROD`, accessed:2016-04-04.

[28] Borlink LS4201S, `http://www.borealisgroup.com/en/polyolefins/products/Borlink/Borlink-LS4201S/`, accessed:2016-03-15.

[29] M. Andersen, An experimental and numerical study of thermoplastics at large deformations, Ph.D. thesis, Norwegian University of Science and Technology, NTNU (2016).

[30] ISO527-2:2012, Plastics - Determination of tensile properties - Part 2: Test conditions for moulding and extrusion plastics, 2012.

[31] Zwick, Temperature chambers, `http://www.zwick.com/en/products/systems-for-climate-and-temperature-testing/temperature-chambers.html`, accessed:2016-03-13.

[32] H. Zhang, Y. Yao, D. Zhu, B. Mobasher, L. Huang, Tensile mechanical properties of basalt fiber reinforced polymer composite under varying strain rates and temperatures, Polymer Testing 51 (2016) 29–39. `doi:10.1016/j.polymertesting.2016.02.006`.

[33] Lexan Exell D, `http://sfs.sabic.eu/product/lexan-solid-sheet/uv-protected/`, accessed:2016-03-21.

[34] T. Børvik, H. Lange, L. A. Marken, M. Langseth, O. S. Hopperstad, M. Aursand, G. Rørvik, Pipe fittings in duplex stainless steel with deviation in quality caused by sigma phase precipitation, Materials Science and Engineering A 527 (26) (2010) 6945–6955. `doi:10.1016/j.msea.2010.06.087`.

[35] Abaqus, 6.13-1, Dassault Systemes, 2013.

[36] ISO22007-4:2008, Plastics - Determination of thermal conductivity and thermal diffusivity - Part 4: Laser flash method, 2008.

[37] MATLAB, Version 8.3.0.532 (R2014a), Natick, Massachusetts, 2014.

[38] V. Aune, E. Fagerholt, K. O. Hauge, M. Langseth, T. Børvik, Experimental study on the response of thin aluminium and steel plates subjected to airblast loading, International Journal of Impact Engineering 90 (2016) 106–121. `doi:10.1016/j.ijimpeng.2015.11.017`.
URL `http://dx.doi.org/10.1016/j.ijimpeng.2015.11.017`

[39] E. Fagerholt, T. Børvik, O. S. Hopperstad, Measuring discontinuous displacement fields in cracked specimens using digital image correlation with mesh adaptation and crack-path optimization, Optics and Lasers in Engineering 51 (3) (2013) 299–310. `doi:10.1016/j.optlaseng.2012.09.010`.
URL `http://dx.doi.org/10.1016/j.optlaseng.2012.09.010`

[40] E. Fagerholt, C. Dørum, T. Børvik, H. I. Laukli, O. S. Hopperstad, Experimental and numerical investigation of fracture in a cast aluminium alloy, International Journal of Solids and Structures 47 (24) (2010) 3352–3365.

doi:10.1016/j.ijsolstr.2010.08.013.

URL http://dx.doi.org/10.1016/j.ijsolstr.2010.
08.013